

# Vortex Thermometry for Turbulent Two-Dimensional Fluids

Andrew J. Groszek,<sup>1</sup> Matthew J. Davis,<sup>2</sup> David M. Paganin,<sup>1</sup> Kristian Helmersen,<sup>1</sup> and Tapio P. Simula<sup>1</sup>

<sup>1</sup>*School of Physics and Astronomy, Monash University, Victoria 3800, Australia*

<sup>2</sup>*School of Mathematics and Physics, University of Queensland, Queensland 4072, Australia*

We introduce a new method of statistical analysis to characterise the dynamics of turbulent fluids in two dimensions. We establish that in equilibrium the vortex distributions can be uniquely connected to the temperature of the vortex gas, and apply this vortex thermometry to characterise simulations of decaying superfluid turbulence. We confirm the hypothesis of vortex evaporative heating leading to Onsager vortices proposed in *Phys. Rev. Lett.* **113**, 165302 (2014), and find previously unidentified vortex power-law distributions which emerge from the dynamics.

Turbulence arises in chaotic dynamical systems across all scales, from mammalian cardiovascular systems, to climate, and even to the formation of stars and galaxies [1]. The unpredictability inherent to turbulent systems is further confounded by physical properties such as boundaries and spatial dimensionality, and due to its complexity, there is currently no unified theoretical framework to explain turbulence. As such, there is a need to develop new methods to characterise the evolution of turbulent states in order to provide further insights into this important problem.

Onsager developed a model of statistical hydrodynamics to describe turbulence in two-dimensional (2D) flows [2]. In this representation the fluid is modelled by an  $N$ -particle gas of interacting point-like vortices which can be characterised by an equilibrium temperature. As the bounded system of vortices has a finite configuration space, the entropy  $S$  of the system has a maximum, and hence there are a range of energies  $E$  where the absolute Boltzmann temperature  $T = (\partial S / \partial E)^{-1}$  becomes negative [2–4]. These states correspond to large scale rotational flows known as Onsager vortices [2].

In driven 2D incompressible fluids negative temperature Onsager states are known to emerge dynamically, effectively giving rise to order from chaos. This peculiar phenomenon is understood to be associated with an inverse energy cascade [5, 6], in which energy flows towards the largest length scales in the system. The inverse cascade arises specifically in 2D as a result of the rigidity of vortex lines, which in the inviscid limit leads to the conservation of enstrophy, the integral of the squared vorticity. In 2D superfluid flows, the picture is more complicated: although the superflow is always inviscid, enstrophy is not conserved due to the possibility of vortex–antivortex annihilation. It is therefore not clear whether the inverse cascade process should carry over into the quantum regime [7]. Despite this, many recent theoretical works involving superfluid Bose–Einstein condensates (BECs) have suggested that large scale, same-sign vortex clusters play an important role in 2D quantum turbulence [8–16]. There has been particular interest in decaying superfluid turbulence, which has been investigated using a variety of concepts including holographic duality [17, 18] and nonthermal fixed points [19–21].

Experimentally, BECs provide unprecedented opportunities to investigate 2D superfluid turbulence due to the high

degree of controllability available in these systems. It is now possible to create and image complex vortex configurations such as dipoles [22–25], few-vortex clusters [26] and quantum von Kármán vortex streets [27]. Many experiments have been devoted to the study of quantum turbulence in both two- [11, 28–30] and three-dimensional [31–33] geometries. However, the formation of Onsager vortex structures in statistical equilibrium has not yet been reported. Recent theoretical works have suggested that one significant obstacle is the harmonic trapping commonly used in experiments, as vortex clusters appear to be suppressed in this geometry [14, 29, 34]. In addition, the detection of vortex circulation signs is experimentally difficult, and only recently have techniques been proposed [35] and implemented [30] to achieve this. Analysis of turbulent dynamics is made even more challenging by current condensate imaging methods, which only allow a small number of frames to be captured for a single experimental realisation [36]. As such, it is desirable to be able to characterise the state of a turbulent fluid using a robust statistical analysis that links the instantaneous microscopic configuration of the system to its macroscopic behaviour. Here we propose to use the vortex temperature as an observable for this purpose.

We first outline our method for measuring the temperature of the vortex gas, before examining a specific case of decaying superfluid turbulence using mean-field Gross–Pitaevskii simulations. In the dynamics, we observe that the vortex gas undergoes rapid equilibration before settling into a quasi-equilibrium state where it continues to heat adiabatically via vortex evaporation [13]. We have discovered that in this evolution, the numbers of clusters, dipoles and free vortices follow robust power-laws with respect to the total vortex number. The existence of this quasi-equilibrium allows quantitative thermometry of the turbulent fluid.

To calibrate the vortex thermometer, we use Monte Carlo (MC) simulations to map out the equilibrium vortex configurations as a function of the inverse temperature  $\beta = 1/k_B T$ , where  $k_B$  is Boltzmann’s constant. We do this for a system of  $N_v = 50$  point vortices with equal numbers of clockwise and anticlockwise circulations. We use a point vortex Hamiltonian corresponding to a uniform fluid within a circular boundary of radius  $R$  [2, 13], and set a hard core of radius  $0.003 R$  to prevent energy divergences. As we vary the temperature across both positive and negative regimes, we quantify the ef-

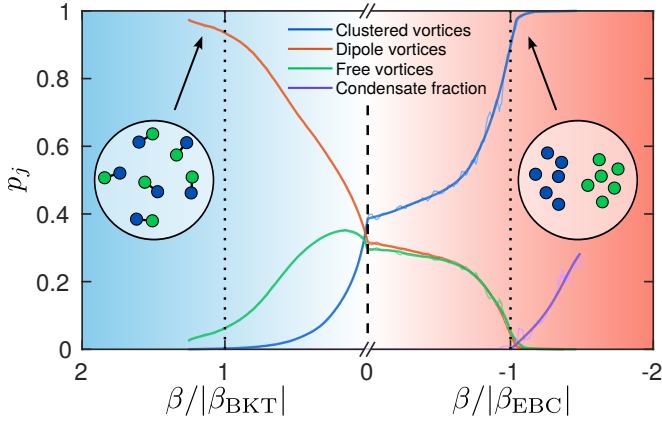


FIG. 1. Fractional population  $p_j = N_j/N_v$  of each component of the vortex gas (where  $j \in \{c: \text{clustered vortices}, d: \text{dipole vortices}, f: \text{free vortices}\}$ ) and Einstein–Bose condensate fraction (described in text), as functions of inverse temperature  $\beta$ . The thin lines show the raw data, while the thick lines show cubic spline fits. The negative temperature axis is scaled by the critical temperature  $|\beta_{\text{EBC}}|$ , and the positive temperature axis by  $|\beta_{\text{BKT}}|$ , causing an apparent discontinuity in the slopes at  $\beta = 0$ . The vertical dashed line indicates  $\beta = 0$  and the dotted vertical lines highlight the two critical temperatures. The shaded background represents the energy of the system (red and blue correspond to ‘hot’/high energy and ‘cold’/low energy, respectively). Schematic vortex configurations at each temperature extreme are depicted in the insets, where vortices (antivortices) are shown as blue (green) dots.

fect on the vortex configuration using a vortex classification algorithm [10, 37]. The algorithm uniquely divides the vortex gas into three separate components: clusters of like-sign vortices, closely bound vortex–antivortex dipoles, and relatively isolated free vortices [38]. We then calculate the numbers of clusters  $N_c$ , dipoles  $N_d$  and free vortices  $N_f$  as functions of temperature, and the resulting fractional population curves are presented in Fig. 1.

At low positive absolute temperatures (left hand side of Fig. 1), the vortex gas is at its ‘coldest’, as both the energy and entropy are minimised. In this regime, bound vortex–antivortex dipole pairs dominate the configuration, as shown in the schematic inset of Fig. 1. Above the Berezinskii–Kosterlitz–Thouless (BKT) critical temperature  $\beta_{\text{BKT}}$ , the vortex dipoles dissociate, causing an increase in both the energy and entropy. At  $\beta = 0$ , the entropy is maximised, but begins decreasing again with temperature in the negative region. In this regime, clusters of like-sign vortices tend to form (as depicted in the schematic inset), and due to their large energy, these negative temperature states are ‘hotter’ than those at positive temperature. Above the critical temperature  $\beta_{\text{EBC}}$ , the vortices form an Einstein–Bose condensate (EBC), a state where the Onsager vortex clusters condense, as indicated by the saturation of the cluster population in Fig. 1 [13, 37, 39]. The two aforementioned critical temperatures are defined as  $\beta_{\text{BKT}} = 2/E_o$  and  $\beta_{\text{EBC}} = -4/N_v E_o$ , respectively, where the energy  $E_o = \rho_s \kappa^2 / 4\pi$  is defined in terms of the superfluid density  $\rho_s$  and the quantum of circulation  $\kappa = h/m$ , with  $m$  being

the mass of the condensed atoms.

Figure 1 demonstrates that the dipole and cluster populations are monotonic functions of  $\beta$ —this is the key observation enabling thermometry of the vortex gas. Given an arbitrary vortex configuration in thermal equilibrium, we may determine its temperature by calculating the mean populations of clusters and/or dipoles and comparing the obtained value to the curves in Fig. 1 [40]. Strictly, the  $p_j(\beta)$  curves in the negative temperature region of Fig. 1 are dependent on the vortex number. However, we repeated our MC simulations for  $N_v = 200$  vortices and found that, for the vortex numbers relevant to the dynamical simulations presented here, the change to the thermometry curves is not significant.

Also shown in Fig. 1 is the Einstein–Bose condensate fraction, which quantifies the density of vortices in the largest cluster (for details, see Ref. [37]). For  $\beta > \beta_{\text{EBC}}$ , the condensate fraction is zero, but when  $\beta < \beta_{\text{EBC}}$  it rises sharply. In this extreme temperature region, the other thermometers saturate and the condensate fraction becomes the relevant order parameter.

As an application of our vortex thermometer, we use it to characterise decaying turbulence in a disk-shaped BEC as previously studied in Refs. [13, 14]. We simulate the two-dimensional time-dependent Gross–Pitaevskii equation (GPE),

$$i\hbar \frac{\partial}{\partial t} \psi = \left[ -\frac{\hbar^2}{2m} \nabla^2 + V_{\text{tr}} + g_{2D} |\psi|^2 \right] \psi, \quad (1)$$

where  $\psi \equiv \psi(\mathbf{r}, t)$  is the classical field of the Bose gas and  $g_{2D}$  is the two-dimensional interaction parameter resulting from the  $s$ -wave atomic collisions. To obtain the uniform circular geometry, we use a two-dimensional power-law trapping potential of the form  $V_{\text{tr}} = \mu(r/R)^{50}$ , where  $r = \sqrt{x^2 + y^2}$  is the radial distance from the axis of the trap,  $\mu$  is the chemical potential, and  $R \approx 171 \xi$  is the radius of the trap, measured in units of the healing length  $\xi = \sqrt{\hbar^2 / 2m\mu}$  [14]. The interaction parameter is set to  $g_{2D} = 4.6 \times 10^4 \hbar^2/m$ . We solve the GPE using a fourth-order split-step Fourier method on a  $1024 \times 1024$  numerical grid with a spacing of approximately  $\xi/2$ . Unless otherwise stated, turbulence is generated by imprinting the vortices into the phase of the superfluid field and the vortex core structures are established by a short imaginary time propagation. We detect vortices and their circulation signs within  $r < 0.98 R$  by locating singularities in the phase of the field.

The initial state for our GPE simulations has  $N_v = 800$  vortices imprinted at random locations with equal numbers of each circulation sign. The short imaginary time evolution causes the loss of  $\sim 40$  vortices, and a further  $\sim 25$  are initiated beyond the detection radius. As the turbulence decays, the vortices annihilate and the vortex gas evaporatively heats, resulting in the emergence of two large Onsager vortices at late times [13, 14]. Three sample frames from a single simulation are shown in Fig. 2, where panels (a)–(c) show the density  $|\psi|^2$  of the fluid, and panels (d)–(f) show the corresponding vortex configuration after the detection and classification

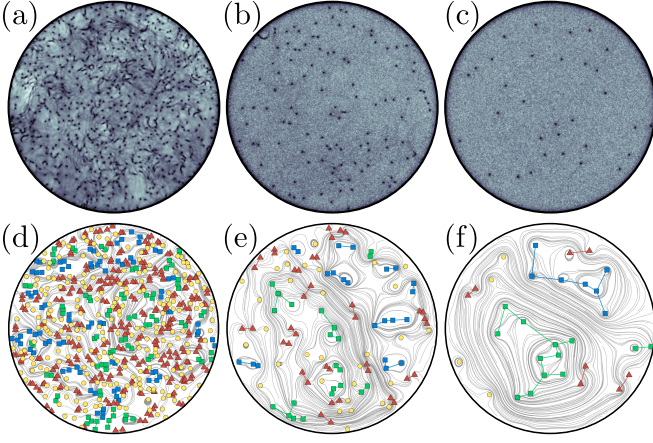


FIG. 2. Freely decaying two-dimensional quantum turbulence. Panels (a)–(c) show the classical field density  $|\psi|^2$ , for respective times  $t \approx (25, 7500 \text{ and } 74000) \hbar/\mu$ , and reveal the vortices as dark spots of zero density. The grayscale in each panel is normalised to the respective peak value of  $|\psi|^2$ . Panels (d)–(f) correspond to panels (a)–(c), respectively, and show the vortices in positive/negative clusters as blue/green squares, dipoles as red triangles, and free vortices as yellow circles. Note that each vortex dipole contains one vortex and one antivortex. The streamlines in (d)–(f) are obtained by calculating the incompressible component of the velocity field of the classical field describing the Bose gas.

steps. A Helmholtz decomposition [8] was used to extract the divergence-free component of the condensate velocity field, and the resulting streamlines are also shown in the lower panels. The Onsager vortex clusters are clearly visible in panel (f).

The evolution of the numbers of clusters, dipoles and free vortices is shown in Fig. 3 as functions of both time  $t$  (see inset) and the total number of vortices  $N_v(t)$ . The time-dependent populations (inset) do not follow any simple function. However, the populations as functions of the total number of vortices (main frame) show clear power-law scaling behaviour. The corresponding power-laws are:

$$N_c \propto N_v^\alpha; \quad N_d \propto N_v^\gamma; \quad N_f \propto N_v^\delta; \quad \text{and} \quad N_{vc} \propto N_v^\varepsilon, \quad (2)$$

with measured values  $\alpha = 0.79$ ,  $\gamma = 1.21$ ,  $\delta = 1.18$ , and  $\varepsilon = -0.25$ . These are suggestive of rational value power-laws with exponents  $\alpha = 4/5$ ,  $\gamma = \delta = 6/5$  and  $\varepsilon = -1/4$ . Here, we have defined the mean number of vortices per cluster as  $N_{vc}(t) \equiv N_c(t)/N_{\text{clus}}(t)$ , where  $N_{\text{clus}}(t)$  is the total number of clusters of any size at a given time. To study the effects of system size on these power-laws, we have also considered two smaller disk-shaped systems of radii  $R \approx 49\xi$  and  $R \approx 85\xi$  respectively, each with  $N_v = 100$  vortices initially imprinted. We find that the scaling behaviour is unchanged in these smaller systems, suggesting that the evolution of the vortex gas is underpinned by a universal microscopic process.

In this system, the primary cause of vortex number decay is the annihilation of vortex–antivortex dipoles [41]. Despite this, the populations of dipoles and free vortices follow approximately the same power-law, demonstrating an intercon-

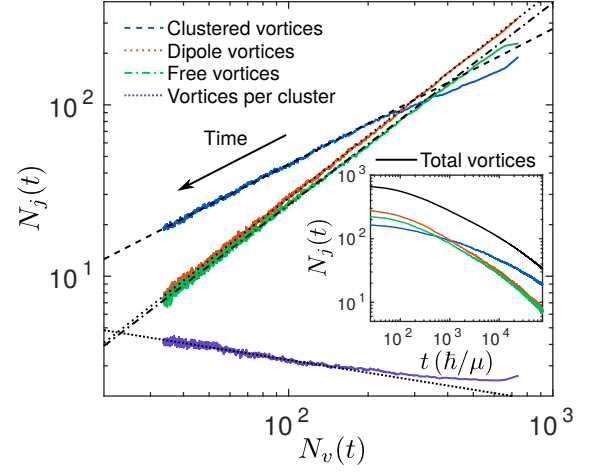


FIG. 3. Decay of the vortex populations  $N_j(t)$  (where  $j \in \{c: \text{clustered vortices}, d: \text{dipole vortices}, f: \text{free vortices}\}$ ) in each component of the vortex gas, and the growth of the number of vortices per cluster  $N_{vc}(t)$ , as functions of the total vortex number  $N_v(t)$ . The data has been averaged over 80 simulations, with power-law fits shown as straight lines. Note that time flows from right to left in this figure. The inset shows the total number of vortices and the number of vortices in each component of the vortex gas as functions of time.

version between the vortex populations. However, a distinct power-law emerges for the vortex clusters. This behaviour points toward a two-fluid model, where the dipoles and free vortices behave as a weakly interacting thermal cloud, while the clusters act as a quasi-condensate whose relative weight grows over time as a result of vortex evaporative heating. This behaviour is a precursor to the Einstein–Bose condensation observed for  $\beta < \beta_{\text{EBC}}$ , which is described in detail in Ref. [37]. Extrapolating the data toward  $N_v \rightarrow 0$  leads to the inevitable decay of all dipoles and free vortices, leaving only Onsager vortex clusters remaining. At this point, the rate of pair annihilation becomes insignificant in the dynamics due to the very low probability of vortex–antivortex collisions.

To assess the sensitivity of the observed power-laws to the choice of initial vortex configuration, we have run simulations with a diverse range of initial conditions. The first of these (case I) is a periodic square array of vortex clusters of alternating circulation sign, each with a radius of  $\sim 43\xi$  and containing  $\sim 50$  vortices. This results in a high kinetic energy configuration. We have also created low energy initial configurations by randomly distributing vortex dipoles of a chosen size throughout the system. For cases II and III, two different initial conditions were chosen with dipoles of sizes  $8\xi$  and  $12\xi$ , respectively (before imaginary time propagation). Finally, for case IV, we have simulated the vortex production dynamically by stirring an initially unperturbed condensate with a repulsive Gaussian potential of waist size  $30\xi$  and amplitude  $5\mu$ . The stirrer was moved back and forth horizontally with centroid position  $x_o(t) = 100\xi \cos(2\pi\mu t/1050\hbar)$  for four periods. The stirring potential was then ramped down linearly to zero over a fifth period.



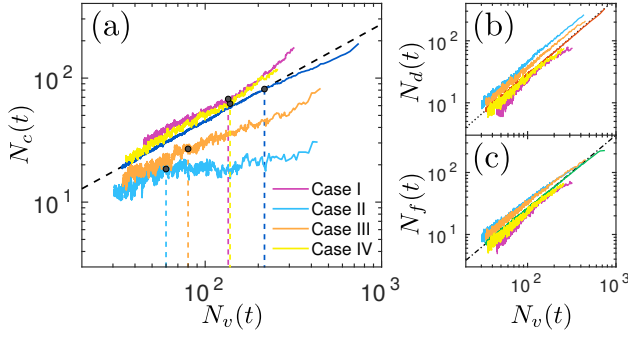


FIG. 4. Vortex decay curves for initial conditions I–IV described in the text, with each curve averaged over ten simulations. The three panels separately show (a) clusters, (b) dipoles, and (c) free vortices. In each subfigure, the corresponding decay curve and power-law fit from Fig. 3 are also shown. In panel (a), dashed vertical lines and black dots indicate the approximate value of  $N_v$  at which each cluster decay curve begins to follow the  $N_c \sim N_v^{4/5}$  power-law.

The resulting number decay curves for each vortex type are shown in Fig. 4(a)–(c), averaged over ten realisations of each initial condition. These curves are shown alongside those from Fig. 3, with each vortex gas component shown separately. The dipole and free vortex decay curves [panels (b) and (c), respectively] remain relatively unchanged across different initial configurations. By contrast, the clusters [panel (a)] show clear variation across the set of initial conditions, suggesting that initially the system is in fact behaving very differently under each constraint. However, despite initial differences (at large  $N_v$ ), all decay curves eventually show the power-law behaviour of Fig. 3, demonstrating the loss of memory of the initial vortex configuration. This suggests that these power-laws correspond to a state of quasi-equilibrium in which the vortex gas should have a well-defined temperature, which we can determine using the thermometers established in Fig. 1.

We now have an algorithm to assign a vortex temperature to the dynamical GPE simulations. We determine the fractional populations of vortex dipoles and clusters as a function of time, and use each of these to read off a temperature from the curves in Fig. 1. The two resulting measurements of  $\beta(t)$  are presented in the main frame of Fig. 5. Both measurements show that the temperature of the vortex gas is spontaneously increasing as Onsager vortex clusters form, thereby confirming the evaporative heating scenario posited in Ref. [13]. At late times, a small discrepancy between the two temperature readings emerges which we attribute to the compressibility of the fluid not included in the MC model.

The inset of Fig. 5 shows the mean temperature readings for the four initial conditions described earlier. These curves show that, at all values of  $N_v$ , both the vortex cluster array and the laser stirred scenarios (cases I and IV, respectively) are at higher negative temperature than the randomly sampled case. By contrast, the dipole initial conditions are the coldest, with the smaller dipoles (II) consistently at a lower

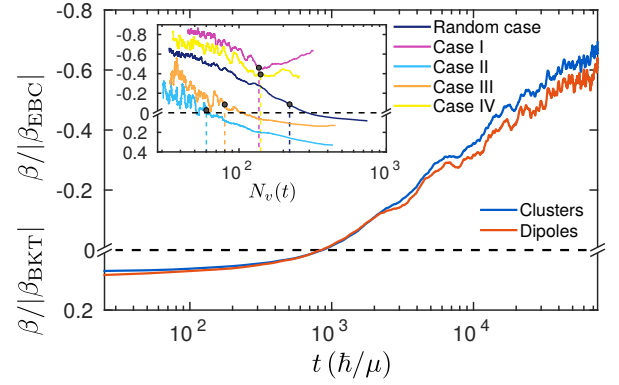


FIG. 5. Inverse temperature of the vortex gas as a function of time, averaged over a set of dynamical GPE simulations. The temperature is measured independently using the populations of both clusters and dipoles. In the inset, the mean temperature readings from both thermometers for cases I–IV (as described in the text) are shown as a function of the total vortex number  $N_v(t)$ , alongside the mean temperature measurement for the randomly sampled case. Vertical dashed lines and black dots to indicate the point at which equilibrium is reached, and should be compared to Fig. 4. As in Fig. 1, the positive and negative temperature regions have been scaled by their respective critical temperatures, and a dashed horizontal line denotes  $\beta = 0$ . The vertical axis of the inset is the same as for the main frame.

temperature than the large dipoles (III), as expected. As in Fig. 4, the approximate value of  $N_v$  at which the vortex gas appears to reach equilibrium in each case is also shown in the inset. Even before this point (i.e. for larger  $N_v$ ), the vortex thermometer provides a plausible temperature reading, but the measurement is not reliable if the vortex gas is out of equilibrium. In cases I and IV, the equilibration point corresponds to a turning point in the temperature curve, providing further evidence for our interpretation of the vortex gas equilibrium condition.

We have developed a methodology that allows the temperature of point vortices in two-dimensional fluids to be determined using only the information about the vortex positions and their signs of circulation. We have applied the vortex gas thermometers to freely decaying two-dimensional quantum turbulent systems and quantitatively shown the transition to negative temperatures and the emergence of Onsager vortices due to the evaporative heating of the vortex gas [13, 14]. Our vortex thermometers may also be useful for characterisation of turbulent classical fluids, as the continuous vorticity distributions can be approximated accurately by a discretised set of point vortices before performing the vortex classification and thermometry. This methodology may therefore open new pathways to quantitative studies of two-dimensional turbulence.

We thank Matthew Reeves for useful feedback on the manuscript. We acknowledge financial support from the Australian Postgraduate Award (A.G.), the Australian Research Council via Discovery Projects DP130102321 (T.S., K.H.), DP170104180 (T.S.), DP160103311 (M.D.) and the nVidia research grant scheme. This research was undertaken with the

assistance of resources from the National Computational Infrastructure (NCI), which is supported by the Australian Federal Government.

- 
- [1] P. A. Davidson, *Turbulence: An Introduction for Scientists and Engineers* (Oxford University Press, 2015).
  - [2] L. Onsager, *Nuovo Cimento* **6**, 279 (1949).
  - [3] E. M. Purcell and R. V. Pound, *Phys. Rev.* **81**, 279 (1951).
  - [4] N. F. Ramsey, *Phys. Rev.* **103**, 20 (1956).
  - [5] R. H. Kraichnan, *Phys. Fluids* **10**, 1417 (1967).
  - [6] R. H. Kraichnan and D. Montgomery, *Rep. Prog. Phys.* **43**, 547 (1980).
  - [7] R. Numasato, M. Tsubota, and V. S. L'vov, *Phys. Rev. A* **81**, 063630 (2010).
  - [8] A. S. Bradley and B. P. Anderson, *Phys. Rev. X* **2**, 041001 (2012).
  - [9] A. C. White, C. F. Barenghi, and N. P. Proukakis, *Phys. Rev. A* **86**, 013635 (2012).
  - [10] M. T. Reeves, T. P. Billam, B. P. Anderson, and A. S. Bradley, *Phys. Rev. Lett.* **110**, 104501 (2013).
  - [11] T. W. Neely, A. S. Bradley, E. C. Samson, S. J. Rooney, E. M. Wright, K. J. H. Law, R. Carretero-González, P. G. Kevrekidis, M. J. Davis, and B. P. Anderson, *Phys. Rev. Lett.* **111**, 235301 (2013).
  - [12] T. P. Billam, M. T. Reeves, B. P. Anderson, and A. S. Bradley, *Phys. Rev. Lett.* **112**, 145301 (2014).
  - [13] T. Simula, M. J. Davis, and K. Helmerson, *Phys. Rev. Lett.* **113**, 165302 (2014).
  - [14] A. J. Groszek, T. P. Simula, D. M. Paganin, and K. Helmerson, *Phys. Rev. A* **93**, 043614 (2016).
  - [15] A. Skaugen and L. Angheluta, *Phys. Rev. E* **93**, 032106 (2016).
  - [16] A. Skaugen and L. Angheluta, *arXiv:1610.04382* (2016).
  - [17] P. M. Chesler, H. Liu, and A. Adams, *Science* **341**, 368 (2013).
  - [18] Y. Du, C. Niu, Y. Tian, and H. Zhang, *J. High Energ. Phys.* **2015**, 1 (2015).
  - [19] B. Nowak, D. Sexty, and T. Gasenzer, *Phys. Rev. B* **84**, 020506 (2011).
  - [20] B. Nowak, J. Schole, D. Sexty, and T. Gasenzer, *Phys. Rev. A* **85**, 043627 (2012).
  - [21] M. Karl and T. Gasenzer, *arXiv:1611.01163* (2016).
  - [22] D. V. Freilich, D. M. Bianchi, A. M. Kaufman, T. K. Langin, and D. S. Hall, *Science* **329**, 1182 (2010).
  - [23] T. W. Neely, E. C. Samson, A. S. Bradley, M. J. Davis, and B. P. Anderson, *Phys. Rev. Lett.* **104**, 160401 (2010).
  - [24] S. Middelkamp, P. J. Torres, P. G. Kevrekidis, D. J. Frantzeskakis, R. Carretero-González, P. Schmelcher, D. V. Freilich, and D. S. Hall, *Phys. Rev. A* **84**, 011605 (2011).
  - [25] W. J. Kwon, S. W. Seo, and Y.-I. Shin, *Phys. Rev. A* **92**, 033613 (2015).
  - [26] R. Navarro, R. Carretero-González, P. J. Torres, P. G. Kevrekidis, D. J. Frantzeskakis, M. W. Ray, E. Altıntaş, and D. S. Hall, *Phys. Rev. Lett.* **110**, 225301 (2013).
  - [27] W. J. Kwon, J. H. Kim, S. W. Seo, and Y. Shin, *Phys. Rev. Lett.* **117**, 245301 (2016).
  - [28] S. J. Rooney, T. W. Neely, B. P. Anderson, and A. S. Bradley, *Phys. Rev. A* **88**, 063620 (2013).
  - [29] W. J. Kwon, G. Moon, J.-Y. Choi, S. W. Seo, and Y.-I. Shin, *Phys. Rev. A* **90**, 063627 (2014).
  - [30] S. W. Seo, B. Ko, J. H. Kim, and Y.-i. Shin, *arXiv:1610.06635* (2016).
  - [31] E. A. L. Henn, J. A. Seman, G. Roati, K. M. F. Magalhães, and V. S. Bagnato, *Phys. Rev. Lett.* **103**, 045301 (2009).
  - [32] P. E. S. Tavares, A. R. Fritsch, G. D. Telles, M. S. Hussein, F. Impens, R. Kaiser, and V. S. Bagnato, *arXiv:1606.01589* (2016).
  - [33] N. Navon, A. L. Gaunt, R. P. Smith, and Z. Hadzibabic, *Nature* **539**, 72 (2016).
  - [34] G. W. Stagg, A. J. Allen, N. G. Parker, and C. F. Barenghi, *Phys. Rev. A* **91**, 013612 (2015).
  - [35] A. T. Powis, S. J. Sammut, and T. P. Simula, *Phys. Rev. Lett.* **113**, 165303 (2014).
  - [36] K. E. Wilson, Z. L. Newman, J. D. Lowney, and B. P. Anderson, *Phys. Rev. A* **91**, 023621 (2015).
  - [37] R. N. Valani, A. J. Groszek, and T. P. Simula, *arXiv:1612.02930* (2016).
  - [38] Any two same-sign vortices are assigned to be in the same cluster if they are closer to each other than either is to an opposite-sign vortex. A dipole is defined as a pair of opposite-sign vortices which are mutual nearest neighbours. After labelling all clusters and dipoles, any vortices remaining are labelled as free vortices. For further details, see Ref. [37].
  - [39] X. Yu, T. P. Billam, J. Nian, M. T. Reeves, and A. S. Bradley, *Phys. Rev. A* **94**, 023602 (2016).
  - [40] The population of free vortices is a non-monotonic function of temperature and is therefore not used for thermometry here.
  - [41] A small proportion are also annihilated at the boundary, as discussed in Ref. [14].